

# First Light And Reionisation Epoch Simulations (FLARES) V: The redshift frontier

Stephen M. Wilkins<sup>1,2\*</sup>, Aswin P. Vijayan<sup>3,4,1</sup>, Christopher C. Lovell<sup>5,1</sup>, William J. Roper<sup>1</sup>, Dimitrios Irodotou<sup>6,1</sup>, Joseph Caruana<sup>2,7</sup>, Louise T. C. Seeyave<sup>1</sup>, Jussi K. Kuusisto<sup>1</sup>, Peter A. Thomas<sup>1</sup>, Shedeur A. K. Parris<sup>1</sup>

<sup>1</sup>*Astronomy Centre, University of Sussex, Falmer, Brighton BN1 9QH, UK*

<sup>2</sup>*Institute of Space Sciences and Astronomy, University of Malta, Msida MSD 2080, Malta*

<sup>3</sup>*Cosmic Dawn Center (DAWN)*

<sup>4</sup>*DTU-Space, Technical University of Denmark, Elektrovej 327, DK-2800 Kgs. Lyngby, Denmark*

<sup>5</sup>*Centre for Astrophysics Research, School of Physics, Astronomy & Mathematics, University of Hertfordshire, Hatfield AL10 9AB, UK*

<sup>6</sup>*Department of Physics, University of Helsinki, Gustaf Hällströmin katu 2, FI-00014, Helsinki, Finland*

<sup>7</sup>*Department of Physics, University of Malta, Msida MSD 2080, Malta*

Accepted XXX. Received YYY; in original form ZZZ

## ABSTRACT

The *James Webb Space Telescope* (*JWST*) is set to transform many areas of astronomy, one of the most exciting is the expansion of the redshift frontier to  $z > 10$ . In its first year alone *JWST* should discover hundreds of galaxies, dwarfing the handful currently known. To prepare for these powerful observational constraints, we use the First Light And Reionisation Epoch (FLARES) simulations to predict the physical and observational properties of the  $z > 10$  population of galaxies accessible to *JWST*. This is the first time such predictions have been made using a hydrodynamical model validated at low redshift. Our predictions at  $z = 10$  are broadly in agreement with current observational constraints on the far-UV luminosity function and UV continuum slope  $\beta$ , though the observational uncertainties are large. We note tension with recent constraints  $z \sim 13$  from Harikane et al. (2021) - compared to these constraints, FLARES predicts objects with the same space density should have an order of magnitude lower luminosity, though this is mitigated slightly if dust attenuation is negligible in these systems. Our predictions suggest that in *JWST*'s first cycle alone, around 600 galaxies should be identified at  $z > 10$ , with the first small samples available at  $z > 13$ .

**Key words:** galaxies: general – galaxies: evolution – galaxies: formation – galaxies: high-redshift – galaxies: photometry

## 1 INTRODUCTION

Identifying and characterising the first generation of galaxies is one of the core aims of modern extragalactic astronomy. Doing so will provide the essential constraints to galaxy formation models, helping us elucidate the key physics of early galaxy formation and evolution (Dayal & Ferrara 2018; Robertson 2021).

Over the last 15 years, remarkable progress has been made in studying the distant Universe, with  $> 1000$  candidate galaxies now identified at  $z = 6 - 10$  (e.g. Bouwens et al. 2021). These have come predominantly from the analysis of deep near-IR observations from Wide Field Camera 3 (WFC3) on the *Hubble Space Telescope* (e.g. Bunker et al. 2010; Bouwens et al. 2010; McLure et al. 2010; Wilkins et al. 2011; Finkelstein et al. 2015; Bouwens et al. 2021), with a small but growing sample of bright sources, more amenable to multi-wavelength follow-up, identified from ground-based imaging (e.g. Bowler et al. 2015). A number of these candidates have now been confirmed by spectroscopy, targeting Ly  $\alpha$  (e.g. Stark et al. 2010; Curtis-Lake et al. 2012; Caruana et al. 2014; Pentericci et al.

2014; Schenker et al. 2014; Stark et al. 2017; Mason et al. 2019) or far-IR lines (e.g. Knudsen et al. 2016; Pentericci et al. 2016; Hashimoto et al. 2019).

While the vast majority of sources are at lower-redshift, a handful of objects have now been detected at  $z > 10$ , often combining *Hubble* and *Spitzer* observations. These include the surprisingly bright galaxy GN-z11 (Oesch et al. 2016) and more recently a pair of candidates at  $z \sim 13$  (Harikane et al. 2021). With the successful launch of the *James Webb Space Telescope* (*JWST*), these sources look set to be only the first of many identified at  $z > 10$  (Robertson 2021). *JWST* offers the sensitivity, survey efficiency, and wavelength coverage to push well beyond the current redshift frontier. In addition, *JWST* will provide rest-frame UV spectroscopy, allowing the confirmation of sources and the accurate measurement of many key physical properties. With the first results from *JWST* imminent, it is essential that we have theoretical predictions in place to allow us to interpret these revolutionary observations.

Theoretical predictions for the high-redshift Universe are available from a variety of modelling approaches. These include semi-empirical methods (e.g. Mason et al. 2015; Behroozi et al. 2020) and semi-analytical models (e.g. Clay et al. 2015; Poole et al. 2016; Yung

\* E-mail: s.wilkins@sussex.ac.uk

et al. 2019; Hutter et al. 2021). However, our most complete understanding comes from hydrodynamical simulations (e.g. Khandai et al. 2012; Feng et al. 2016; Vogelsberger et al. 2020; Ni et al. 2022), particularly those incorporating full radiative transfer (RT) (e.g. O’Shea et al. 2015; Ocvirk et al. 2016; Rosdahl et al. 2018; Ocvirk et al. 2020; Kannan et al. 2022).

The main drawback of hydrodynamical simulations - especially those including RT - is that they are computationally expensive, limiting their volume, resolution, and/or redshift end point. This is a particular problem at very high redshift, where the source density is so low that simulations comparable to, and ideally much larger, observational surveys are essential to yield useful statistical predictions. Indeed, flagship cosmological simulations that have been validated at low-redshift, like EAGLE (Schaye et al. 2015; Crain et al. 2015), SIMBA (Davé et al. 2019), ILLUSTRIS (Vogelsberger et al. 2014a,b; Genel et al. 2014; Sijacki et al. 2015), and ILLUSTRIS-TNG (Naiman et al. 2018; Nelson et al. 2018; Marinacci et al. 2018; Springel et al. 2018; Pillepich et al. 2018) fail to pass this threshold, with only a small number of observationally accessible sources at  $z > 10$ .

One solution is to carry out much larger simulations, but limited to high-redshift. This is a strategy implemented by, e.g., MASSIVEBLACK (Khandai et al. 2012), BLUETIDES (Feng et al. 2016; Wilkins et al. 2017), and ASTRID (Ni et al. 2022). An alternative strategy is to *re-simulate* a range of environments drawn from a very large low-resolution parent simulation (e.g. Crain et al. 2009). This has the advantage of more efficiently allowing us to extend the dynamic range (see discussion in Lovell et al. 2021). These individual re-simulations are also much smaller than single large boxes, allowing wider and more efficient use of HPC systems. The chief disadvantages are the loss of most clustering information and the requirement to carefully understand the weightings of the individual simulations to obtain the correct statistical properties of the galaxy population. Machine learning approaches may allow us to overcome some of these limitations (e.g. Lovell et al. 2022; Bernardini et al. 2022).

Re-simulations of multiple regions is utilised in the FLARES: First Light And Reionisation Epoch Simulations project. FLARES combines the validated at  $z = 0$  EAGLE physics model with a re-simulation strategy yielding a much larger effective volume and dynamic range. Compared to the  $(100 \text{ Mpc})^3$  EAGLE reference simulation, FLARES contains 10-100 $\times$  as many high-redshift galaxies. In this article we use FLARES to make predictions for the galaxy population at  $z > 10$ , building on earlier work focused at  $z = 5 - 10$  (Lovell et al. 2021; Vijayan et al. 2021, 2022; Roper et al. 2022).

This article is organised as follows: in Section 2 we briefly describe the FLARES project. In Section 3 we explore the physical properties of galaxies at  $z > 10$  and in Section 4 explore their observational properties, including the UV luminosity function and forecasts for upcoming surveys (§4.1), the UV continuum slope  $\beta$  (§4.3), UV emission lines (§4.4), and the UV - optical colours (§4.5). Finally, in Section 5 we present our conclusions.

## 2 THE FIRST LIGHT AND REIONISATION EPOCH SIMULATIONS

In this study, we make use of the First Light And Reionisation Epoch Simulations (FLARES; Lovell et al. 2021; Vijayan et al. 2021). FLARES is a suite of 40 spherical re-simulations,  $14 h^{-1} \text{ Mpc}$  in radius, of regions selected from a large  $(3.2 \text{ Gpc})^3$  dark matter only simulation. The regions selected to re-simulate span a range of en-

vironments: (at  $z \approx 4.7$ )  $\log_{10}(1 + \delta_{14}) = [-0.3, 0.3]^1$  with over-representation of the extremes of the density contrast distribution.

FLARES adopts the AGNdT9 variant of the EAGLE simulation project (Schaye et al. 2015; Crain et al. 2015). The AGNdT9 variant implements a higher heating temperature from active galactic nuclei (AGN) compared to the reference EAGLE run, thus producing more energetic, less frequent feedback events. We adopt identical resolution to the fiducial EAGLE simulation, i.e. dark matter and initial gas particle masses of  $m_{\text{dm}} = 9.7 \times 10^6 M_{\odot}$  and  $m_{\text{g}} = 1.8 \times 10^6 M_{\odot}$ , respectively, and a softening length of 2.66 ckpc. As with the original EAGLE simulations, we assume  $\Omega_{\text{m}} = 0.307$ ,  $\Omega_{\Lambda} = 0.693$ ,  $h = 0.6777$  based on results from Planck Collaboration et al. (2014).

Galaxies in FLARES are first identified as groups via the Friends-Of-Friends (FOF, Davis et al. 1985) algorithm, and subsequently subdivided into bound groups with the SUBFIND (Springel et al. 2001; Dolag et al. 2009) algorithm. When measuring properties we use 30 kpc radius apertures, centred on the most bound particle of each subgroup.

### 2.1 Spectral Energy Distribution Modelling

Key to making observational predictions is the spectral energy distribution (SED) modelling applied to the simulation outputs. The SED modelling approach is presented in Vijayan et al. (2021), broadly following the approach developed by Wilkins et al. (2013b, 2016c, 2018, 2020), with modifications to the dust treatment. In short, we begin by associating each star particle with *pure stellar* spectral energy distribution (SED) using v2.2.1 of the Binary Population and Spectral Synthesis (BPASS; Stanway & Eldridge 2018) stellar population synthesis model assuming a Chabrier (2003) initial mass function (IMF). We then associate each star particle with HII region giving rise to nebular continuum and line emission. Specifically, we follow the approach detailed in Wilkins et al. (2020), in which the pure stellar spectrum is processed with the cloudy photo-ionisation code (Ferland et al. 2017). We account for the effects of dust attenuation in both the birth clouds of young stellar populations and the interstellar medium (ISM). The latter is accounted for using a line-of-sight (LOS) model similar to that described in Wilkins et al. (2018). In this model we treat stellar particles as emitters along a line of sight and account for the attenuation due to gas particles which intersect this LOS. To do this we determine the metal column density and convert this to a dust optical depth using the fitting function for the dust-to-metal ratio presented in Vijayan et al. (2019). For the attenuation due to the birth cloud component, we scale it with the star particle metallicity, thus assuming a constant dust-to-metal ratio. The proportionality factors for the two components are fixed to match the  $z = 5$  UV LF from Bouwens et al. (2015),  $z = 5$  UV-continuum slope relations and the [OIII] $\lambda$ 4959, 5007 + H $\beta$  line luminosity and EW relations at  $z = 8$  from De Barros et al. (2019a).

### 2.2 Comparison to EAGLE

The core objective of FLARES is to expand both number and dynamic range of simulated galaxies at  $z > 5$  compared to the EAGLE reference simulation. The number of galaxies in both FLARES and EAGLE with stellar mass greater than  $\in \{10^8, 10^9, 10^{10}, 10^{11}\} M_{\odot}$  at  $z > 5$  are shown in Fig. 1. At  $z = 10$  FLARES contains 100 $\times$  ( $10\times$ ) as many galaxies as EAGLE with  $M_{\star} > 10^9 M_{\odot}$  ( $M_{\star} > 10^8 M_{\odot}$ ). At

<sup>1</sup> Where  $\delta_{14}$  is the density contrast measured within the re-simulation volume size.

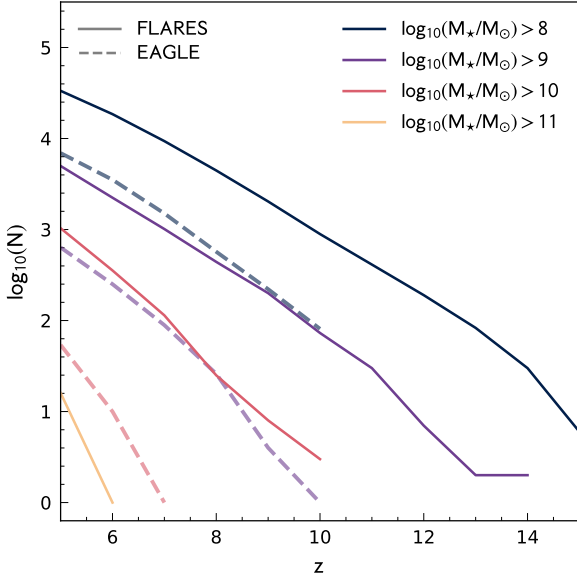


**Figure 1.** The number of galaxies in EAGLE (dashed line) and FLARES (solid line) at  $z > 5$  above various stellar mass limits.

$z = 10$  FLARES contains  $\sim 1000$  galaxies at  $M_* > 10^8 M_\odot$ , dropping to 10 by  $z = 15$ .

### 2.3 Environmental dependence

A key feature of FLARES is the explicit simulation of a wide range of environments with  $\log_{10}[1 + \delta_{14}(z = 4.7)] \approx [-0.3, 0.3]$ . In Lovell et al. (2021) we showed that the galaxy stellar mass function, and thus the total number of galaxies above a mass threshold, was extremely sensitive to the environment. A consequence of this, and the low number density of galaxies at  $z > 10$ , is that the vast majority of our simulated galaxies are in very over-dense regions as shown in Fig. 2. At  $z = 15$  only one simulation with  $\delta < 0.5$  contains any galaxies. Since each simulation is appropriately weighted (see Lovell et al. 2021) the lack of any galaxies in many density contrast bins should not affect distribution functions like the galaxy stellar mass function or UV luminosity function. However, if galaxy scaling relationships are sensitive to the environment, even the appropriately weighted relations could be biased. Fortunately, Lovell et al. (2021) found no significant evidence of environmental dependence in the key scaling relations.

## 3 PHYSICAL PROPERTIES

We begin by exploring a selection of key physical properties of galaxies at  $z > 10$ . In Fig. 3 we show the relationship between stellar mass and the specific star formation rate, age, gas-phase metallicity, and far-UV dust attenuation. At present, there are no observational constraints for these properties but this should soon change.

The relationship between stellar mass and specific star formation rate is predicted to be fairly flat, though with significant redshift evolution of the normalisation. Similarly, the average age - defined here as the time since its stellar mass was half its current value - is flat with stellar mass but evolves strongly with redshift. At  $z = 10$ , the

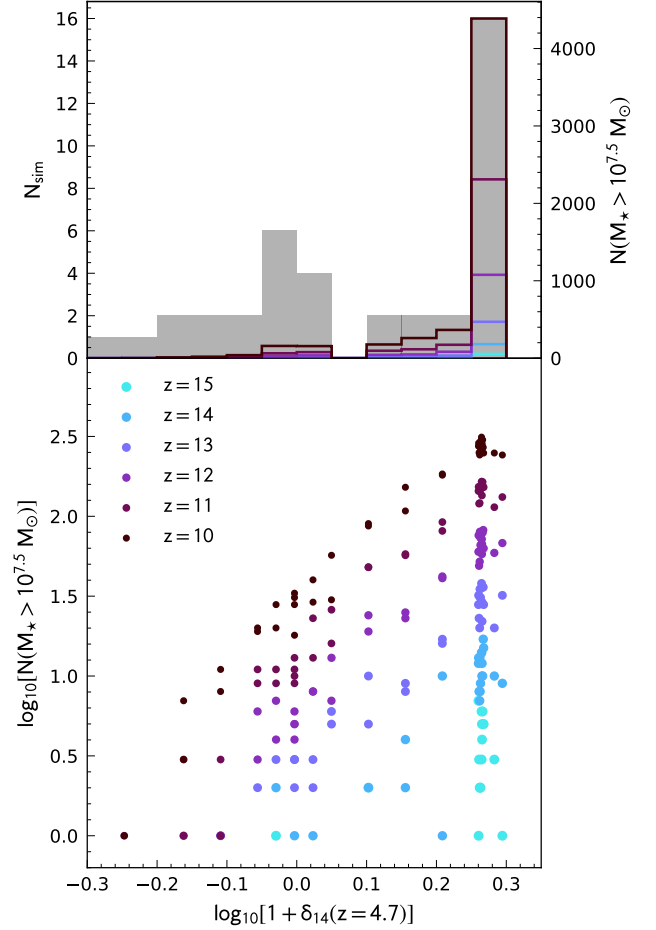


**Figure 2.** *Bottom-panel:* The number of  $M_* > 10^{7.5} M_\odot$  galaxies in each individual simulation as a function of density contrast. *Top-panel:* The number of individual simulations (grey filled histogram) and  $M_* > 10^{7.5} M_\odot$  galaxies in density contrast bins.

average age is predicted to be  $\approx 20$  Myr rising to almost  $\approx 100$  Myr at  $z = 10$ .

On the other hand, the gas phase metallicity  $Z_g$  shows a significant trend with stellar mass but little redshift evolution. Similarly we see a strong trend between the far-UV attenuation and stellar mass but little redshift evolution. Given the gas phase metallicity trends this is unsurprising since the attenuation in FLARES is related to surface density of metals.

### 3.1 Mass-to-light ratio

One of the most fundamental properties is the mapping between stellar mass and the (dust-attenuated) far-UV luminosity. This encodes the star formation and metal enrichment history of each galaxy in addition to reprocessing by dust and gas. This relationship is shown in Fig. 4. At  $M_* < 10^{8.5} M_\odot$  this relationship is close to linear; at high-masses, however, the luminosity falls below the linear expectation. This is predominantly due to the effects of dust, but is also affected by the higher stellar metallicities in the most massive galaxies. The

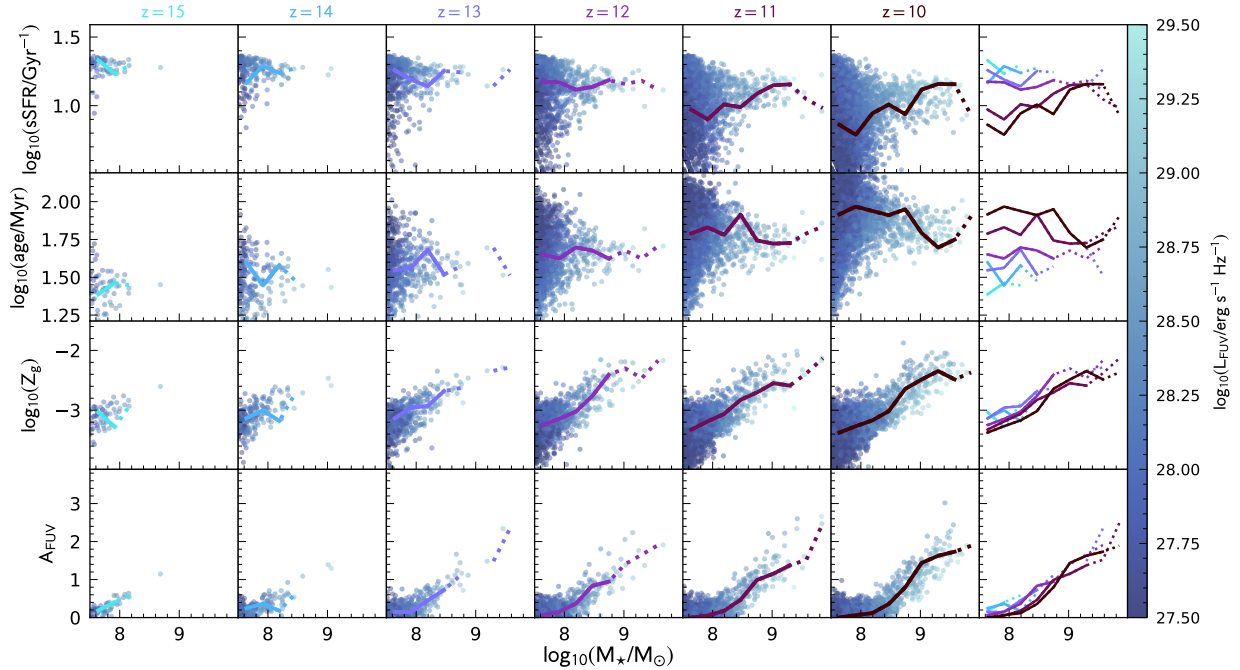


**Figure 3.** The predicted physical properties as a function of stellar mass at  $z = 15 \rightarrow 10$ . The line on each panel shows the weighted median, i.e. accounting for the statistical weights of each re-simulation. Where the number of galaxies in each bin falls below 10 the median is denoted by a dotted line. The final panel summarises the redshift evolution of the median. Individual galaxies are coloured by their far-UV luminosity.

scatter in this relationship is  $\approx 0.2$  dex independent of redshift and stellar mass.

## 4 OBSERVATIONAL PROPERTIES

We now turn our attention to some of the properties of galaxies that can be observed at  $z > 10$ . *JWST* will, for the first time, provide deep  $>2 \mu\text{m}$  imaging and spectroscopy allowing us to measure several properties including the rest-frame UV luminosity (and thus luminosity function), the UV continuum slope, UV emission lines, and potentially even UV - optical colours via MIRI imaging. Model spectral energy distributions of star forming galaxies at  $z = 10$  and  $z = 15$  are shown, alongside the *JWST* filter transmission functions in Fig. 5.

### 4.1 Far-UV luminosity function

The rest-frame far-UV luminosity function (LF) is one of the key statistical descriptions of the galaxy population at high-redshift. This is predominantly due to its accessibility but also the fact that the observed UV light traces both unobscured star formation (Kennicutt & Evans 2012; Wilkins et al. 2019) and the production of ionising photons (Wilkins et al. 2016b). The far-UV LF has now been measured extensively to  $z \sim 8$  with tentative constraints at  $\sim 10$  (e.g. McLeod et al. 2016; Oesch et al. 2018; Finkelstein et al. 2021) and more recently at  $z \sim 13$  (Harikane et al. 2021).

In Fig. 6 we show the far-UV luminosity predicted by FLARES at  $z = 15 \rightarrow 10$  alongside both these observational constraints and other model predictions. We show both the *observed* (dust-attenuated) and *intrinsic* distribution functions. The far-UV LF follows the familiar steep decline with luminosity seen at low-redshift, dropping

by roughly a factor of  $10^3$  from  $L = 10^{28} \rightarrow 10^{29} \text{ erg s}^{-1} \text{ Hz}^{-1}$ . The number density of sources also evolves strongly, increasing by  $\sim 10\times$  from  $z = 14 \rightarrow 10$  with stronger evolution at the bright end. At low-luminosity ( $L < 10^{28.5} \text{ erg s}^{-1} \text{ Hz}^{-1}$ ) the impact of dust is small leaving the intrinsic and observed LF similar. However, as noted previously brighter, more massive galaxies, increasingly have stronger dust attenuation leading to a divergence in the predictions.

The  $z = 10$  panel shows current observational constraints from McLeod et al. (2016), Oesch et al. (2018), and Finkelstein et al. (2021) all based on *Hubble*/WFC3 observations. While the observational uncertainties are large McLeod et al. (2016) and Oesch et al. (2018) bracket the FLARES predictions; the Oesch et al. (2018) constraints falling slightly below the predictions at low luminosities. The Finkelstein et al. (2021) constraints lie at the bright end of our predictions where dust attenuation is predicted to become important. These constraints agree better with the FLARES intrinsic predictions, possibly suggesting that too much dust is assumed in FLARES at this redshift.

Shown on the  $z = 13$  panel are the recent observational constraints from Harikane et al. (2021). This study used observations from Hyper Suprime-Cam, VISTA, and *Spitzer* of the COSMOS and SXDS fields to identify a pair of bright sources with spectral energy distribution consistent with  $z \sim 13$  star forming galaxies. In addition, one source has a tentative line detection consistent with [OIII]88 $\mu\text{m}$  at  $z = 13.27$ , in-line with its photometric redshift. If real these sources suggest little evolution in the bright end of the UV luminosity function from  $z \sim 10 \rightarrow 13$ . FLARES contains objects with a similar space density as these sources but with dust-attenuated luminosities around a factor of  $10\times$  smaller. As noted, at  $z > 10$  the FLARES dust model is likely to become increasingly unreliable since it is based on modelling calibrated at lower-redshift. However, even using in-

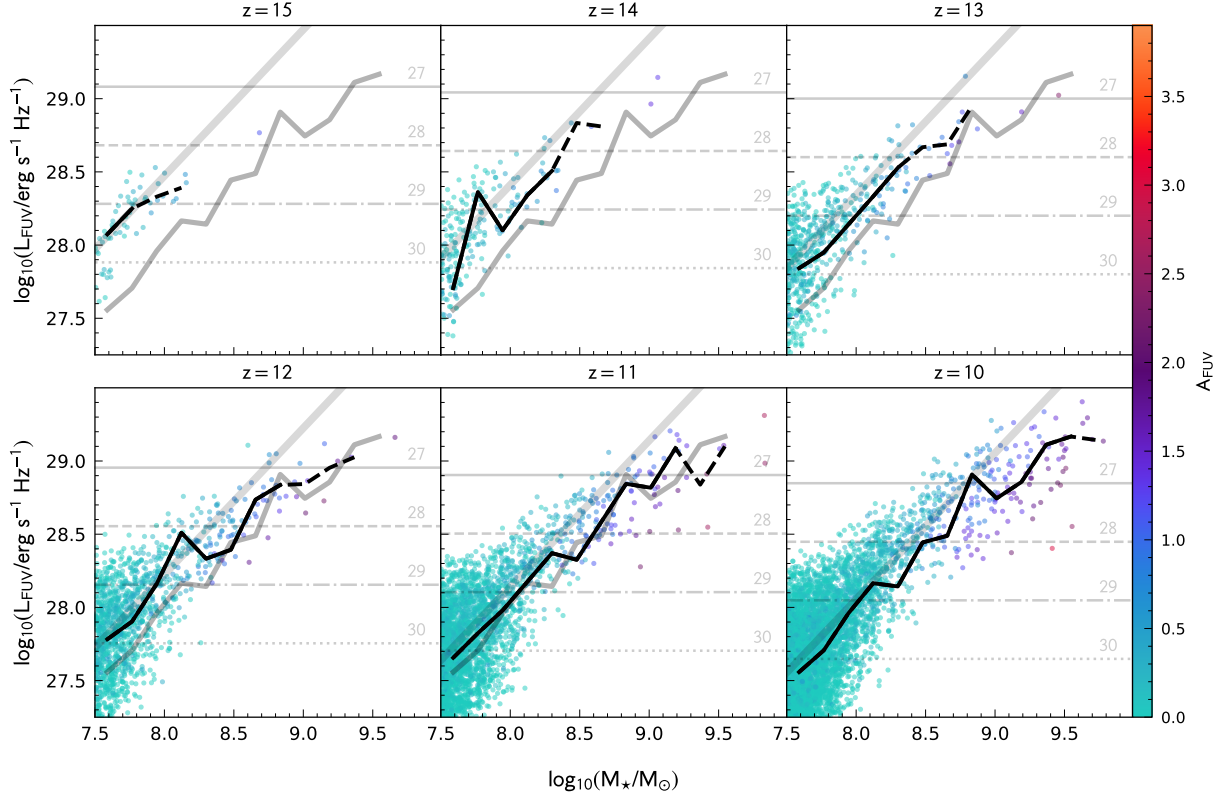


**Figure 4.** The relationship between stellar mass and the dust-attenuated (observed) far-UV luminosity at  $z = 15 \rightarrow 10$ . Points are colour-coded by the far-UV attenuation  $A_{\text{FUV}}$ . The black line denotes the weighted median at each redshift with the line becoming dashed when the number of galaxies in each bin falls below 10. The thin grey line shows the median at  $z = 10$ . The thick grey line shows a weighted linear fit. Horizontal lines denote the corresponding apparent magnitude.

$\log_{10}(L_{\text{FUV}})$ $\text{erg s}^{-1} \text{Hz}^{-1}$	$\phi/\text{Mpc}^{-3} \text{dex}^{-1}$					
	$z = 15$	$z = 14$	$z = 13$	$z = 12$	$z = 11$	$z = 10$
27.8	-4.16	-3.59	-3.14	-2.78	-2.53	-2.37
28.0	-4.10	-3.64	-3.35	-3.02	-2.92	-2.67
28.2	-4.67	-4.47	-3.64	-3.45	-3.29	-3.19
28.4	-5.07	-4.71	-4.33	-4.29	-4.07	-3.65
28.6	-7.04	-6.01	-4.95	-4.83	-4.60	-4.33
28.8	-7.45	-6.71	-6.29	-5.02	-4.88	-4.56
29.0	-	-7.45	-6.12	-6.06	-5.14	-4.64
29.2	-	-6.20	-7.04	-6.12	-6.04	-4.82
29.4	-	-	-	-	-7.22	-6.68

**Table 1.** The space density of galaxies at  $z = 10 \rightarrow 15$  predicted by FLARES.

trinsic luminosities, sources with a similar space density in FLARES are still around  $5\times$  fainter, suggesting significant remaining tension.

Fig. 6 also shows a comparison with other model predictions at  $z \geq 10$  including the semi-empirical model of Mason et al. (2015), the Santa Cruz semi-analytical model (Yung et al. 2019), the large volume cosmological hydrodynamical simulation BLUETIDES (Wilkins et al. 2017), and the high-resolution FIRE-2 simulations (Ma et al. 2019). While there is good agreement at  $z = 10$ , the agreement with Mason et al. (2015) and BLUETIDES breaks down at high-redshift; FLARES predicts a similar density of bright galaxies but consistently predicts more faint galaxies.

#### 4.1.1 JWST Cycle 1 forecasts

As noted in the introduction the  $z > 10$  galaxy population will soon be accessible via several deep imaging surveys conducted by JWST. Using our luminosity function predictions we can now forecast the number of sources expected for each survey and the eventual constraints on the  $z = 10 - 15$  LF.

We begin, in Fig. 7, by presenting forecasts for the cumulative number of sources accessible to various JWST Cycle 1 GO, ERS, and GTO programmes. These include: CEERS, NG-DEEP<sup>2</sup>, PRIMER, COSMOS-Web<sup>3</sup>, JADES, the Northern Ecliptic Pole element of PEARLS<sup>4</sup>, and PANORAMIC. These predictions assume 100% completeness down to the  $10\sigma$  point-source F277W depth, which in reality is likely to be difficult to achieve. The approximate depths/areas for each survey were provided by each programme PI except for JADES which are taken from Williams et al. (2018). Across all 7 programmes we predict  $\sim 500$ , 85, and 6 galaxies at  $z > 10$ ,  $z > 12$ , and  $z > 14$  respectively. JADES is predicted to dominate these numbers contributing around half of expected sources at these redshifts.

In Fig. 8 we then make forecasts for the  $z = 15 \rightarrow 10$  luminosity function for the combination of the Cycle 1 programmes. The result is strong constraints at  $z = 10$ , comparable to the current  $z = 7$  con-

<sup>2</sup> Formerly Webb DEEP.

<sup>3</sup> Formerly COSMOS-Webb.

<sup>4</sup> Formerly the Webb Medium Deep Fields programme (PI Windhorst).

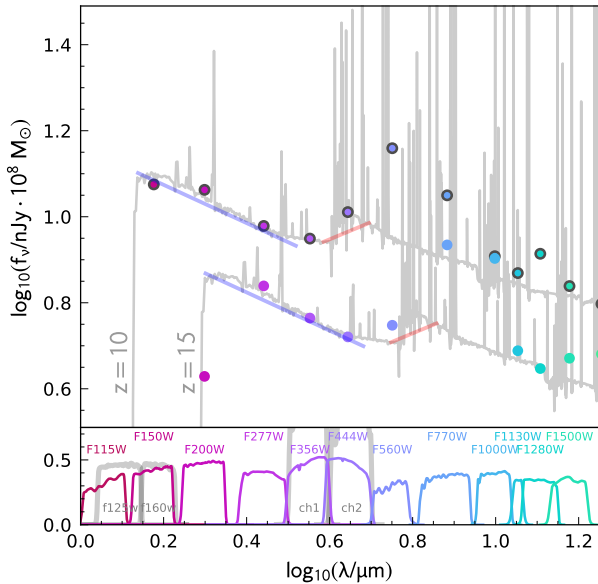


**Figure 5.** The observed spectral energy distribution of a star forming galaxy at  $z = 10$  and  $z = 15$  alongside key *Hubble*, *Spitzer*, *JWST*/NIRCam, and *JWST*/MIRI filter transmission functions. Coloured points denote the predicted fluxes in each of the NIRCam and MIRI bands highlighting the impact of nebular emission in the rest-frame optical. The blue and red lines denote the UV continuum slope and Balmer break respectively.

straints from *Hubble*'s entire campaign (Bouwens et al. 2021). While these constraints progressively weaken toward higher redshift subsequent observations throughout *JWST*'s tenure should ultimately enable useful constraints to  $z \sim 15$  and potentially beyond. Crucially this will allow us to differentiate between the different model predictions in this era.

## 4.2 Sizes

In Fig. 9 we present measurements of galaxy half light radius in the far-UV for  $z = 10 - 12$ . The intrinsic size measurements are derived from the particle distribution, while the observed size measurements use a non-parametric pixel approach in which size is derived from the non-contiguous pixel area containing half the galaxy's total luminosity. The latter approach well encompasses the clumpy natures of high redshift galaxies (e.g Jiang et al. 2013; Bowler et al. 2017). The redshift range is limited by the number of galaxies in FLARES with a sufficient number of stellar particles to make robust size measurements ( $N_* \geq 100$ ). As in Roper et al. (2022) we impose a 95 percent completeness limit in each redshift bin.

Intrinsically the high redshift galaxy population is extremely compact with a negative size-luminosity relation. However, the bright central regions of these compact galaxies are also efficiently seeding their surroundings with metals, even at this early epoch. This seeding leads to strong dust obscuration in the brightest regions, and thus a large increase in the observed size and a positive observed size-luminosity relation. The normalisation of the observed size-luminosity relation quickly evolves at these high redshifts, with an increase of  $\sim 0.1$  dex from  $z = 12$  to  $z = 10$  driven by increasing obscuration of the brightest regions due to the formation of dust in the highly star forming cores of these bright galaxies. *JWST* will not

only be able to probe this obscured size-luminosity relation in the rest frame far-UV, the reddest NIRCam filters will also be able to probe deeper into the increasingly unobscured size-luminosity relation at longer wavelength. This will provide a valuable view into the intrinsic size-luminosity relation and its negative slope.

## 4.3 The UV continuum slope

The most accessible spectral diagnostic available at high-redshift is the UV continuum slope  $\beta$ : as can be seen in Fig. 5 the rest-frame UV continuum to  $\lambda = 350$  nm is accessible to NIRCam to  $z \approx 15$  and can be measured with 3-4 of NIRCam's wide filters. While primarily an indicator of dust attenuation the UV continuum slope is also sensitive to the star formation and metal enrichment history, the Lyman continuum escape fraction, the initial mass function, and our understanding of stellar evolution and atmospheres<sup>5</sup> (e.g Wilkins et al. 2013b,a).

Fig. 10 shows predictions for  $\beta$  from  $z = 15 \rightarrow 10$  colour coded by the rest-frame far-UV attenuation. At  $L_{\text{FUV}} < 10^{28.5} \text{ erg s}^{-1} \text{ Hz}^{-1}$  ( $M_{\text{FUV}} > -19.5$ ) the slope is  $\approx -2.4$  with little evolution with redshift. At  $L_{\text{FUV}} > 10^{28.5} \text{ erg s}^{-1} \text{ Hz}^{-1}$  the slope progressively reddens due to the increasing dust attenuation. At  $L_{\text{FUV}} > 10^{29} \text{ erg s}^{-1} \text{ Hz}^{-1}$  the average slope has reddened to  $\approx -2$ . Fig. 10 also shows observational constraints from Wilkins et al. (2016a); while the uncertainties are large these observations are consistent with our predictions.

The origin of the UV continuum slope is explored in more detail in Fig. 11. Here we show the median  $\beta$  for unprocessed starlight (dotted line), starlight with reprocessing by gas (dashed line), and reprocessing with gas and dust (solid line, the same as that shown in Fig. 10). With no reprocessing the predicted slopes are  $\approx -2.8$  at low-luminosity rising to  $\approx -2.5$  at  $L_{\text{FUV}} \approx 10^{29.5} \text{ erg s}^{-1} \text{ Hz}^{-1}$  with some weak ( $\Delta\beta = 0.1$ ) evolution with redshift  $z = 15 \rightarrow 10$ . These trends reflect variation in the star formation and metal enrichment history with the brightest galaxies typically having higher metallicities. The addition of nebular (continuum) emission reddens  $\beta$ . As the impact of nebular emission is strongest at low metallicity this has the effect of flattening the previous trend with luminosity and redshift leaving galaxies with  $\beta \approx 2.5$ . The addition of dust has an impact at all luminosities though this is most pronounced at  $L_{\text{FUV}} > 10^{29} \text{ erg s}^{-1} \text{ Hz}^{-1}$  where dust is predicted to redden the slope by  $\approx 0.5$ .

As noted previously the impact of dust attenuation in FLARES is particularly uncertain at  $z > 10$ . Recent luminosity function constraints (i.e. Finkelstein et al. 2021; Harikane et al. 2021) tentatively suggest the presence of too much dust attenuation in FLARES. Precise constraints on the UV continuum slope from *JWST* - and ideally ALMA dust continuum observations - in bright ( $L_{\text{FUV}} > 10^{29} \text{ erg s}^{-1} \text{ Hz}^{-1}$ ) should allow us to determine whether this is the case.

## 4.4 UV emission lines

In addition to deep near-IR imaging, *JWST* will also be able to obtain deep near-IR spectroscopy utilising NIRSpec, NIRCam, and NIRISS<sup>6</sup>. NIRSpec provides both a multi-object and integral field

<sup>5</sup> In a theoretical context this is encapsulated in stellar population synthesis models.

<sup>6</sup> MIRI also has spectroscopic capabilities but has much lower sensitivity and only target galaxies individually.

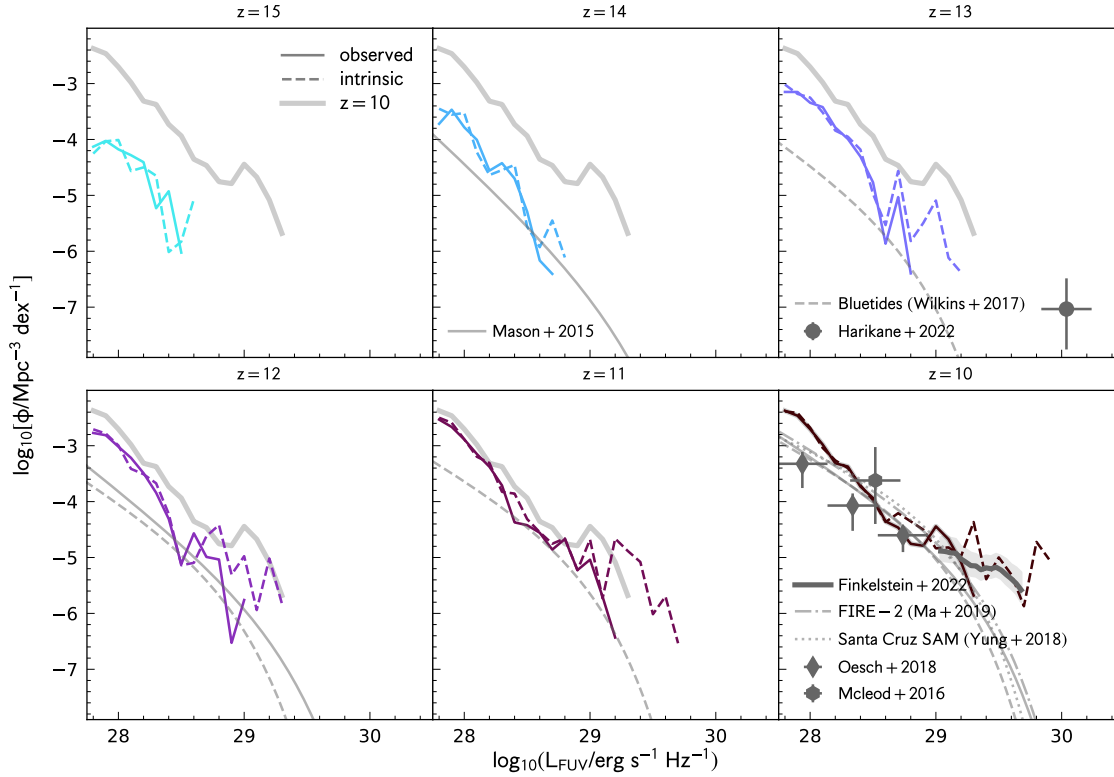


**Figure 6.** The observed (dust-attenuated, solid line) and intrinsic (dashed line) far-UV luminosity function at  $z = 15 \rightarrow 10$  predicted by FLARES. The thick grey line denotes the  $z = 10$  prediction to more clearly demonstrate the redshift evolution. Observational constraints at  $z = 10$  and  $z = 13$  from [McLeod et al. \(2016\)](#), [Oesch et al. \(2018\)](#), [Finkelstein et al. \(2021\)](#), and [Harikane et al. \(2021\)](#) are also shown. Model predictions from [Mason et al. \(2015\)](#), [Wilkins et al. \(2017\)](#), [Yung et al. \(2019\)](#), and [Ma et al. \(2019\)](#) are also shown where available. These FLARES binned luminosity functions are available in Table 1.

unit spectroscopy at  $0.6\text{--}5.3\mu\text{m}$ , while NIRCcam and NIRISS together provide wide field slit-less spectroscopy across the near-IR. At  $z < 10$  this enables the observation of various strong optical lines. However, at  $z > 10$  most of the strong lines fall outside the accessible range leaving a handful of weaker UV lines. Most prominent amongst these is the  $[\text{CIII}], \text{CIII}] \lambda \lambda 1907, 1909\text{\AA}$  doublet for which a handful of detections are already available at  $z > 6$  ([Stark et al. 2015, 2017; Topping et al. 2021](#)).

Predictions from FLARES for the rest-frame equivalent width distribution of  $[\text{CIII}], \text{CIII}]$  are presented in Fig. 12 as a function of the observed (dust attenuated) far-UV luminosity. Equivalent widths show a weak decline to higher luminosity and lower-redshift. The median value is  $\approx 10\text{\AA}$  with the tail of the distribution reaching beyond  $20\text{\AA}$ . Unsurprisingly, given the younger age, these predictions are offset to higher equivalent widths than observations at lower redshift (e.g [Maseda et al. 2017; Llerena et al. 2022](#)). Constraints at  $z > 6$  include a handful of detections and upper-limits and are likely biased due to their selection method. However, two of the detections: EGS-zs8-1 ([Stark et al. 2017](#)) and AEGIS-33376 ([Topping et al. 2021](#)) have equivalent widths at the upper extreme of the predicted distribution suggesting some possible tension. This may reflect some of the simplifying assumptions used in our modelling. For example, [Wilkins et al. \(2020\)](#) showed that the equivalent width of  $[\text{CIII}], \text{CIII}]$  is strongly sensitive to the ionisation parameter and hydrogen density, for which we adopted single fiducial values.

#### 4.5 UV - Optical colours

The near-UV - optical colour is another key spectral diagnostic of galaxies, its measurement providing insights into the star formation and metal enrichment history, dust attenuation, and nebular emission of galaxies. In the context of  $z > 6$  galaxies the near-UV - optical colour is chiefly impacted by nebular line emission and can be used to infer the strength of combination of the  $\text{H}\beta$  and  $[\text{OIII}]$  lines (e.g [De Barros et al. 2019b; Endsley et al. 2021](#)). Where a spectroscopic redshift is available it is sometimes possible to avoid strong line emission providing "clean" constraints on the strength of the Balmer break (e.g [Hashimoto et al. 2018](#)) and thus a more accurate constraint on the star formation and metal enrichment history. For a wider introduction to the break in the context of the high-redshift Universe see [Wilkins et al. in-prep](#).

In principle *JWST* can observe the rest-frame optical to  $z = 15$  and beyond. However, at  $z > 11$  the optical falls beyond the range accessible to *JWST*'s near-IR instruments and thus requires MIRI observations. Several blind-field cycle 1 surveys will simultaneously collect both multi-band NIRCcam and MIRI imaging. For MIRI F770W is the most popular choice and with this in mind we present the predicted F444W-F770W colour in Fig. 13. We do this for both the pure stellar photometry and the photometry including nebular emission and dust. In both cases there is little trend with the UV luminosity. The addition of nebular emission (and dust) has the impact of significantly reddening the colour by  $\approx 0.4$  mag at  $z = 10$  increasing to  $\approx 0.7$  mag at  $z = 15$ . This reflects both the increasing optical line equivalent widths but also the lines that fall within the F770W band.

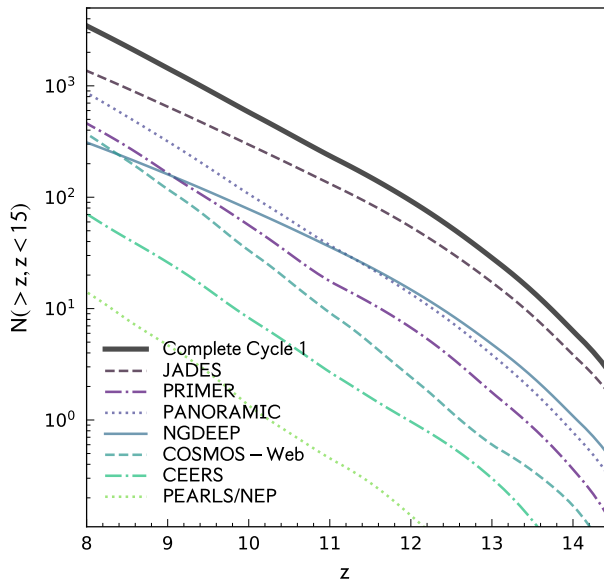


**Figure 7.** The cumulative number of galaxies  $N(> z, z < 15)$  predicted by FLARES for various JWST Cycle 1 GO, ERS, and GTO surveys assuming 100% completeness down to the  $10\sigma$  point-source F277W depth. The thick black line denotes the prediction for all surveys combined.

While in principle, MIRI observations, when combined with NIRCam, should thus allow us to constrain optical line emission at  $z > 10$ , unfortunately MIRI has both a lower sensitivity<sup>7</sup> and smaller field-of-view than NIRCam resulting in a much reduced survey efficiency. Blind field cycle 1 programmes (i.e. PRIMER, COSMOS-Web, CEERS) obtaining both NIRCam and MIRI F770W observations typically reach depths F770W 3 magnitudes shallower than the deepest NIRCam observations and only over less than half the total area. Combined with the expected surface densities and flux distributions it is then unlikely, even with stacking, that MIRI will yield useful constraints at  $z > 10$ . However, there is the possibility of obtaining deep MIRI imaging of individual bright targets in later cycles.

## 5 CONCLUSIONS

In this article we have presented theoretical predictions for the properties of galaxies at  $z = 10 - 15$  from the FLARES: First Light And Reionisation Epoch Simulations. These are amongst the first predictions from a cosmological hydrodynamical simulation calibrated at  $z = 0$  at these redshifts enabled by the unique simulation strategy adopted by FLARES. Our major findings are:

- Specific star formation rates and ages show little trend with stellar mass though evolve strongly with redshift. However, gas-phase metallicities and dust attenuation rapidly increase with stellar mass but show little redshift evolution.

<sup>7</sup> In 10 ks NIRCam can reach in 9.1 nJy and 23.6 nJy in the F200W and F444W bands respectively while for the MIRI F560W and F770W bands the flux sensitivity is 130 nJy and 240 nJy.

- The far-UV luminosity function continues its evolution from lower-redshift with the luminosity density predicted to drop by  $\sim 10\times$  from  $z = 10 \rightarrow 14$ . At  $z = 10$  the predictions are consistent with observational constraints from McLeod et al. (2016), Oesch et al. (2018), and Finkelstein et al. (2021) though favour less dust attenuation. FLARES contains galaxies with a similar space density to those recently identified by Harikane et al. (2021) but  $\sim 5 - 10\times$  fainter depending on whether dust attenuation is included. Similarly agreement with other models is good at  $z = 10$  but diverges to higher-redshift with FLARES predicting more faint galaxies than other models. Based on these predictions in cycle 1 alone JWST should identify  $\sim 600, 100,$  and  $6$  galaxies at  $z > 10, 12,$  and  $14$  respectively providing robust constraints on the LF to  $z \sim 13$ .

- FLARES predicts little redshift evolution in the relationship between the UV continuum slope  $\beta$  and UV luminosity. The brightest galaxies are predicted to be moderately reddened ( $\Delta\beta \approx 0.5$ ) by dust.

- UV-optical colours probed by NIRCam and MIRI are likely to be dominated by nebular emission though will be hard to measure due to MIRI's much lower sensitivity.

## ACKNOWLEDGEMENTS

We dedicate this article to healthcare and other essential workers, the teams involved in developing the vaccines, and to all the parents who found themselves having to home-school children while holding down full-time jobs. We thank the EAGLE team for their efforts in developing the EAGLE simulation code. This work used the DiRAC@Durham facility managed by the Institute for Computational Cosmology on behalf of the STFC DiRAC HPC Facility ([www.dirac.ac.uk](http://www.dirac.ac.uk)). The equipment was funded by BEIS capital funding via STFC capital grants ST/K00042X/1, ST/P002293/1, ST/R002371/1 and ST/S002502/1, Durham University and STFC operations grant ST/R000832/1. DiRAC is part of the National e-Infrastructure. CCL acknowledges support from the Royal Society under grant RGF/EA/181016. DI acknowledges support by the European Research Council via ERC Consolidator Grant KETJU (no. 818930). The Cosmic Dawn Center (DAWN) is funded by the Danish National Research Foundation under grant No. 140. We also wish to acknowledge the following open source software packages used in the analysis: NUMPY (Harris et al. 2020), SCIPY (Virtanen et al. 2020), and MATPLOTLIB (Hunter 2007). This research made use of ASTROPY <http://www.astropy.org> a community-developed core Python package for Astronomy (Astropy Collaboration et al. 2013, 2018). Parts of the results in this work make use of the colormaps in the CMASHER package (van der Velden 2020).

## DATA AVAILABILITY STATEMENT

Binned data for making easy comparisons is available in ascii formats at [https://github.com/stephenmwilkins/flares\\_frontier\\_data](https://github.com/stephenmwilkins/flares_frontier_data). Data from the wider FLARES project is available at <https://flaresimulations.github.io/data.html>. If you use data from this paper please also cite Lovell et al. (2021) and Vijayan et al. (2021).

## REFERENCES

- Astropy Collaboration et al., 2013, *A&A*, **558**, A33  
 Astropy Collaboration et al., 2018, *AJ*, **156**, 123  
 Behroozi P., et al., 2020, *MNRAS*, **499**, 5702

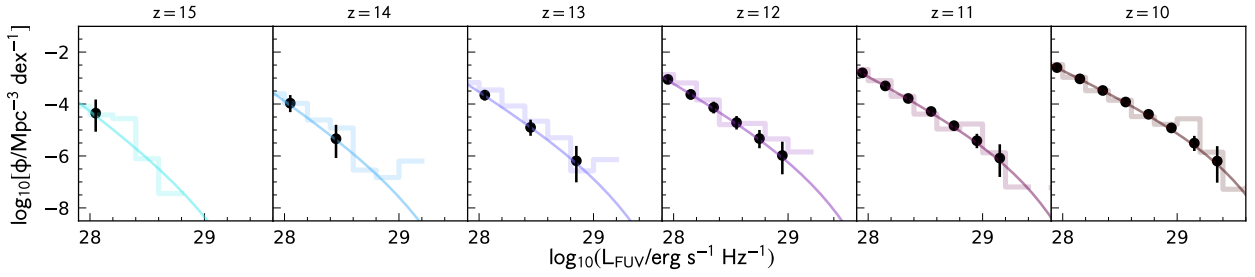


**Figure 8.** Predicted constraints on the UV  $z = 15 \rightarrow 10$  UV luminosity function from combined JWST Cycle 1 GO, ERS, and GTO surveys. Points show the forecast binned LF constraints. The stepped line shows the FLARES binned LF constraints while the smooth lines show Schechter function fits to the FLARES LF.

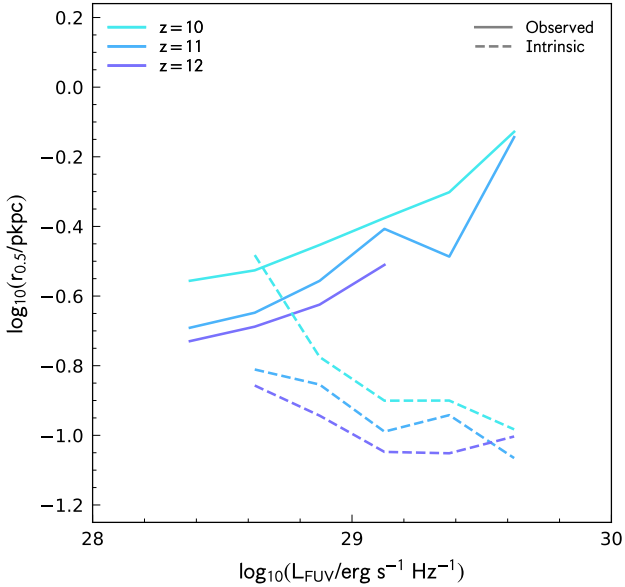


**Figure 9.** The redshift evolution of the size - luminosity relation predicted by FLARES in the redshift range  $z = 10 - 12$ . The lines represent the weighted 50th percentile of the galaxy distribution weighted using the FLARES weighting scheme. Solid lines show the observed size including the effects of dust attenuation, while dashed lines show the intrinsic stellar emission. Observed sizes are measured using a non-parametric pixel approach while intrinsic sizes use a particle based approach.

Bernardini M., Feldmann R., Anglés-Alcázar D., Boylan-Kolchin M., Bullock J., Mayer L., Stadel J., 2022, *MNRAS*, **509**, 1323  
 Bouwens R. J., et al., 2010, *ApJ*, **709**, L133  
 Bouwens R. J., et al., 2015, *ApJ*, **803**, 34  
 Bouwens R. J., et al., 2021, *AJ*, **162**, 47  
 Bowler R. A. A., et al., 2015, *MNRAS*, **452**, 1817  
 Bowler R. A. A., Dunlop J. S., McLure R. J., McLeod D. J., 2017, *MNRAS*, **466**, 3612  
 Bunker A. J., et al., 2010, *MNRAS*, **409**, 855  
 Caruana J., Bunker A. J., Wilkins S. M., Stanway E. R., Lorenzoni S., Jarvis M. J., Ebert H., 2014, *MNRAS*, **443**, 2831  
 Chabrier G., 2003, *PASP*, **115**, 763  
 Clay S. J., Thomas P. A., Wilkins S. M., Henriques B. M. B., 2015, *MNRAS*, **451**, 2692  
 Crain R. A., et al., 2009, *MNRAS*, **399**, 1773  
 Crain R. A., et al., 2015, *MNRAS*, **450**, 1937  
 Curtis-Lake E., et al., 2012, *MNRAS*, **422**, 1425

Davé R., Anglés-Alcázar D., Narayanan D., Li Q., Rafieferantsoa M. H., Appleby S., 2019, *MNRAS*, **486**, 2827  
 Davis M., Efstathiou G., Frenk C. S., White S. D. M., 1985, *ApJ*, **292**, 371  
 Dayal P., Ferrara A., 2018, *Phys. Rep.*, **780**, 1  
 De Barros S., Oesch P. A., Labbé I., Stefanon M., González V., Smit R., Bouwens R. J., Illingworth G. D., 2019a, *MNRAS*, **489**, 2355  
 De Barros S., Oesch P. A., Labbé I., Stefanon M., González V., Smit R., Bouwens R. J., Illingworth G. D., 2019b, *MNRAS*, **489**, 2355  
 Dolag K., Borgani S., Murante G., Springel V., 2009, *MNRAS*, **399**, 497  
 Endsley R., Stark D. P., Chevallard J., Charlot S., 2021, *MNRAS*, **500**, 5229  
 Feng Y., Di-Matteo T., Croft R. A., Bird S., Battaglia N., Wilkins S., 2016, *MNRAS*, **455**, 2778  
 Ferland G. J., et al., 2017, *Rev. Mex. Astron. Astrofis.*, **53**, 385  
 Finkelstein S. L., et al., 2015, *ApJ*, **810**, 71  
 Finkelstein S. L., et al., 2021, arXiv e-prints, p. arXiv:2106.13813  
 Genel S., et al., 2014, *MNRAS*, **445**, 175  
 Harikane Y., et al., 2021, arXiv e-prints, p. arXiv:2112.09141  
 Harris C. R., et al., 2020, *Nature*, **585**, 357  
 Hashimoto T., et al., 2018, *Nature*, **557**, 392  
 Hashimoto T., et al., 2019, *PASJ*, **71**, 71  
 Hunter J. D., 2007, *Computing in Science & Engineering*, **9**, 90  
 Hutter A., Dayal P., Yepes G., Gottlöber S., Legrand L., Ucci G., 2021, *MNRAS*, **503**, 3698  
 Jiang L., et al., 2013, *ApJ*, **773**, 153  
 Kannan R., Garaldi E., Smith A., Pakmor R., Springel V., Vogelsberger M., Hernquist L., 2022, *MNRAS*, **511**, 4005  
 Kennicutt R. C., Evans N. J., 2012, *ARA&A*, **50**, 531  
 Khandai N., Feng Y., DeGraf C., Di Matteo T., Croft R. A. C., 2012, *MNRAS*, **423**, 2397  
 Knudsen K. K., Richard J., Kneib J.-P., Jauzac M., Clément B., Drouart G., Egami E., Lindroos L., 2016, *MNRAS*, **462**, L6  
 Llerena M., et al., 2022, *A&A*, **659**, A16  
 Lovell C. C., Vijayan A. P., Thomas P. A., Wilkins S. M., Barnes D. J., Irodotou D., Roper W., 2021, *MNRAS*, **500**, 2127  
 Lovell C. C., Wilkins S. M., Thomas P. A., Schaller M., Baugh C. M., Fabian G., Bahé Y., 2022, *MNRAS*, **509**, 5046  
 Ma X., et al., 2019, *MNRAS*, **487**, 1844  
 Marinacci F., et al., 2018, *MNRAS*, **480**, 5113  
 Maseda M. V., et al., 2017, *A&A*, **608**, A4  
 Mason C. A., Trenti M., Treu T., 2015, *ApJ*, **813**, 21  
 Mason C. A., et al., 2019, *MNRAS*, **485**, 3947  
 McLeod D. J., McLure R. J., Dunlop J. S., 2016, *MNRAS*, **459**, 3812  
 McLure R. J., Dunlop J. S., Cirasuolo M., Koekemoer A. M., Sabbi E., Stark D. P., Targett T. A., Ellis R. S., 2010, *MNRAS*, **403**, 960  
 Naiman J. P., et al., 2018, *MNRAS*, **477**, 1206  
 Nelson D., et al., 2018, *MNRAS*, **475**, 624  
 Ni Y., et al., 2022, *MNRAS*,  
 O'Shea B. W., Wise J. H., Xu H., Norman M. L., 2015, *ApJ*, **807**, L12  
 Ocvirk P., et al., 2016, *MNRAS*, **463**, 1462  
 Ocvirk P., et al., 2020, *MNRAS*, **496**, 4087  
 Oesch P. A., et al., 2016, *ApJ*, **819**, 129

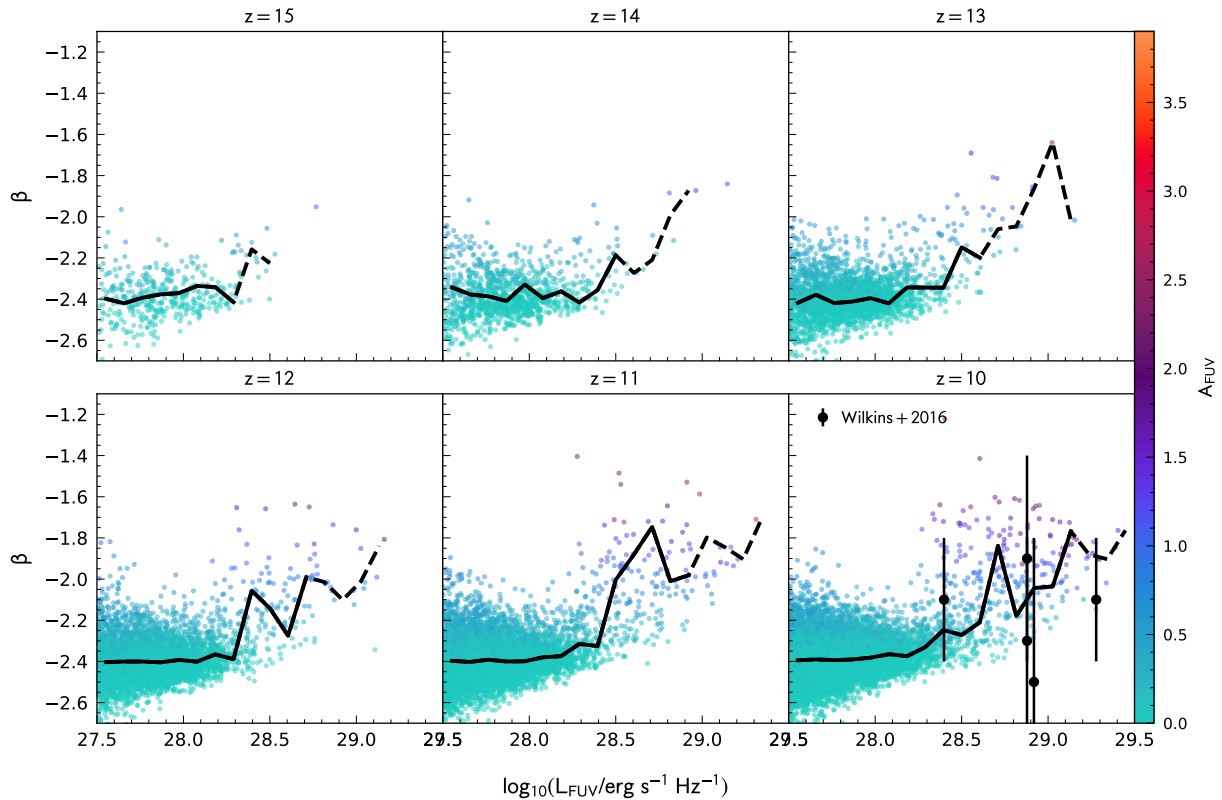


**Figure 10.** The rest-frame UV continuum slope  $\beta$  as a function of far-UV luminosity at  $z = 15 \rightarrow 10$ . Individual galaxies are coloured by their far-UV attenuation. The solid (dashed) black line shows the median value for bins with  $\geq 10$  ( $< 10$ ) galaxies. Observational constraints from Wilkins et al. (2016a) are also shown at  $z = 10$ .

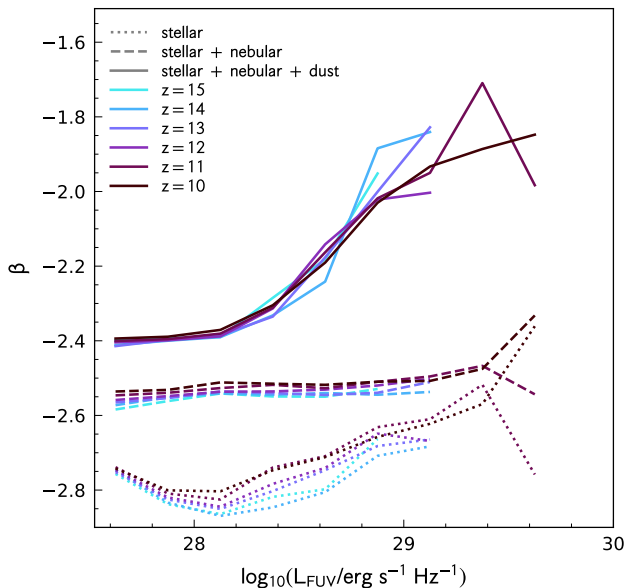


**Figure 11.** The average UV continuum slope as a function of UV luminosity and redshift. The dotted line shows the UV continuum slope predicted from just the pure stellar emission, the dashed line including nebular emission, and the solid line also including dust (i.e. that which would be observed).

- Oesch P. A., Bouwens R. J., Illingworth G. D., Labbé I., Stefanon M., 2018, *ApJ*, **855**, 105
- Pentericci L., et al., 2014, *ApJ*, **793**, 113
- Pentericci L., et al., 2016, *ApJ*, **829**, L11
- Pillepich A., et al., 2018, *MNRAS*, **475**, 648
- Planck Collaboration et al., 2014, *A&A*, **571**, A1
- Poole G. B., Angel P. W., Mutch S. J., Power C., Duffy A. R., Geil P. M., Mesinger A., Wyithe S. B., 2016, *MNRAS*, **459**, 3025
- Robertson B. E., 2021, arXiv e-prints, p. arXiv:2110.13160
- Roper W. J., Lovell C. C., Vijayan A. P., Marshall M. A., Irodotou D., Kuusisto J. K., Thomas P. A., Wilkins S. M., 2022, arXiv e-prints, p. arXiv:2203.12627
- Rosdahl J., et al., 2018, *MNRAS*, **479**, 994
- Schaye J., et al., 2015, *MNRAS*, **446**, 521
- Schenker M. A., Ellis R. S., Konidaris N. P., Stark D. P., 2014, *ApJ*, **795**, 20
- Sijacki D., Vogelsberger M., Genel S., Springel V., Torrey P., Snyder G. F., Nelson D., Hernquist L., 2015, *MNRAS*, **452**, 575
- Springel V., White S. D. M., Tormen G., Kauffmann G., 2001, *MNRAS*, **328**, 726
- Springel V., et al., 2018, *MNRAS*, **475**, 676
- Stanway E. R., Eldridge J. J., 2018, *MNRAS*, **479**, 75
- Stark D. P., Ellis R. S., Chiu K., Ouchi M., Bunker A., 2010, *MNRAS*, **408**, 1628
- Stark D. P., et al., 2015, *MNRAS*, **450**, 1846
- Stark D. P., et al., 2017, *MNRAS*, **464**, 469
- Topping M. W., Shapley A. E., Stark D. P., Endsley R., Robertson B., Greene J. E., Furlanetto S. R., Tang M., 2021, *ApJ*, **917**, L36
- Vijayan A. P., Clay S. J., Thomas P. A., Yates R. M., Wilkins S. M., Henriques B. M., 2019, *MNRAS*, **489**, 4072
- Vijayan A. P., Lovell C. C., Wilkins S. M., Thomas P. A., Barnes D. J.,

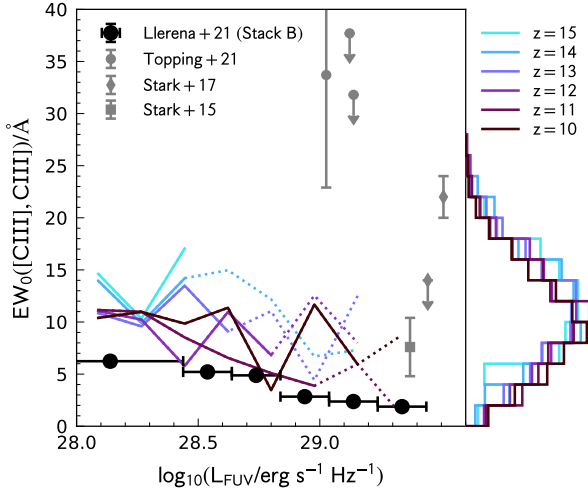


**Figure 12.** The distribution of [CIII],CIII] $\lambda\lambda$  1907, 1909 $\text{\AA}$  equivalent widths at  $z = 10 - 15$  predicted by FLARES. Also shown are stacked results at  $z \approx 3$  from the VANDELS survey (Llerena et al. 2022) and individual objects at  $z > 6$  (Stark et al. 2015, 2017; Topping et al. 2021).

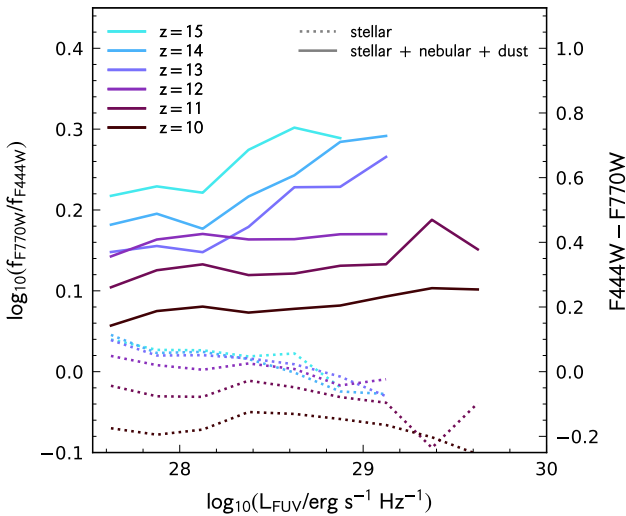


**Figure 13.** The average NIRCcam/F444W - MIRI/F770W colour as a function of UV luminosity for both the pure stellar emission (dotted line) and including nebular emission and dust (solid line).

Irodotou D., Kuusisto J., Roper W. J., 2021, *MNRAS*, **501**, 3289  
 Vijayan A. P., et al., 2022,  
 Virtanen P., et al., 2020, *Nature Methods*, **17**, 261  
 Vogelsberger M., et al., 2014a, *MNRAS*, **444**, 1518  
 Vogelsberger M., et al., 2014b, *Nature*, **509**, 177  
 Vogelsberger M., et al., 2020, *MNRAS*, **492**, 5167  
 Wilkins S. M., Bunker A. J., Lorenzoni S., Caruana J., 2011, *MNRAS*, **411**, 23  
 Wilkins S. M., Bunker A., Coulton W., Croft R., di Matteo T., Khandai N., Feng Y., 2013a, *MNRAS*, **430**, 2885  
 Wilkins S. M., et al., 2013b, *MNRAS*, **435**, 2885  
 Wilkins S. M., Bouwens R. J., Oesch P. A., Labbé I., Sargent M., Caruana J.,

Wardlow J., Clay S., 2016a, *MNRAS*, **455**, 659  
 Wilkins S. M., Feng Y., Di-Matteo T., Croft R., Stanway E. R., Bouwens R. J., Thomas P., 2016b, *MNRAS*, **458**, L6  
 Wilkins S. M., Feng Y., Di-Matteo T., Croft R., Stanway E. R., Bunker A., Waters D., Lovell C., 2016c, *MNRAS*, **460**, 3170  
 Wilkins S. M., Feng Y., Di Matteo T., Croft R., Lovell C. C., Waters D., 2017, *MNRAS*, **469**, 2517  
 Wilkins S. M., Feng Y., Di Matteo T., Croft R., Lovell C. C., Thomas P., 2018, *MNRAS*, **473**, 5363  
 Wilkins S. M., Lovell C. C., Stanway E. R., 2019, *MNRAS*, **490**, 5359  
 Wilkins S. M., et al., 2020, *MNRAS*, **493**, 6079  
 Williams C. C., et al., 2018, *ApJS*, **236**, 33  
 Yung L. Y. A., Somerville R. S., Finkelstein S. L., Popping G., Davé R., 2019, *MNRAS*, **483**, 2983  
 van der Velden E., 2020, *The Journal of Open Source Software*, **5**, 2004

This paper has been typeset from a  $\text{\TeX}/\text{\LaTeX}$  file prepared by the author.